

See discussions, stats, and author profiles for this publication at: <https://www.researchgate.net/publication/275235285>

Polythienylene–Vinylene Structure–Function Correlations Revealed from Resonance Raman Spectroscopy and Photocurrent Imaging

ARTICLE in THE JOURNAL OF PHYSICAL CHEMISTRY C · APRIL 2015

Impact Factor: 4.77 · DOI: 10.1021/acs.jpcc.5b02166

CITATION

1

READS

38

7 AUTHORS, INCLUDING:



Jian Gao

Lawrence Berkeley National Laboratory

16 PUBLICATIONS 102 CITATIONS

SEE PROFILE



Cody Ryan Aldaz

University of Michigan

1 PUBLICATION 1 CITATION

SEE PROFILE



John K Grey

University of New Mexico

26 PUBLICATIONS 397 CITATIONS

SEE PROFILE

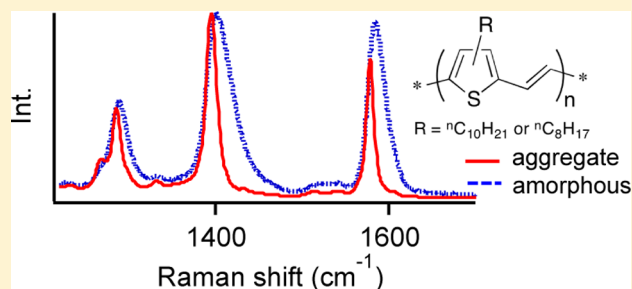
Polythienylene–Vinylene Structure–Function Correlations Revealed from Resonance Raman Spectroscopy and Photocurrent Imaging

Jian Gao, Alan K. Thomas, Jianzhang Yang, Cody Aldaz, Guoshun Yang, Yang Qin, and John K. Grey*

Department of Chemistry and Chemical Biology, University of New Mexico, Albuquerque, New Mexico 87131, United States

S Supporting Information

ABSTRACT: New structure–function correlations are revealed in poly(3-alkyl-thienylenevinylene) (P3ATV) derivatives using resonance Raman spectroscopy techniques. P3ATVs are prototype conjugated polymers that have received increased attention recently due to reports of efficient singlet fission following excitation of the lowest energy allowed (1B_u) excited state. Raman spectra are measured with excitation wavelengths resonant with the P3ATV 1B_u absorption line shape (~ 450 – 750 nm) to probe geometrical rearrangements incurred in this initial excited state. Rich spectral features are resolved, namely, multiple overtone and combination progressions involving the main P3ATV symmetric skeletal stretching vibrational modes. We use a time-dependent wavepacket approach to calculate the Raman cross-correlation wavepacket overlap function for each displaced mode and their extent of displacement in the excited state. Fit parameters are checked by simulating optical absorption spectra that show good agreement with experimental absorption line shapes. Excitation wavelength-dependent Raman frequency dispersion and Raman excitation profiles of symmetric CC skeletal vibrations showed significant variation across the P3ATV absorption envelope and anomalously large enhancements for lower energy (longer wavelength) excitation, respectively. We demonstrate these behaviors are due to excitation of aggregated and amorphous P3ATV chains with distinct absorption and Raman signatures. This assignment was confirmed by measuring Raman spectra to selectively excite each limiting form and spectral decomposition of absorption line shapes using simulated absorption spectra of aggregates. Resonance Raman and photocurrent imaging of model P3ATV/fullerene blend solar cells were next performed to spatially correlate local morphology to photocurrent generation efficiency. Raman images of aggregated and amorphous P3ATV regions were constructed that show larger photocurrent production in the former, suggesting these structures are well mixed with PCBM. Conversely, amorphous zones have diminished PCBM content, resulting in lower photocurrents. Absorption and Raman spectra demonstrate that the P3ATV aggregate packing characteristics and amounts are largely unaffected by the addition of PCBM, indicating weak interactions with P3ATV chain backbone that lead to poor charge generation efficiencies in solar cells.



INTRODUCTION

Solar cells based on conjugated polymer donor and fullerene acceptor blends have demonstrated enormous potential as candidates for efficient and inexpensive alternative energy resources.^{1–4} Despite large improvements in device performance and lifetime, there is still room for improvement since power conversion efficiencies are often well below theoretical limits. Ideally, there should be minimal losses of the incident photon energy; however, efficient nonradiative excited state deactivation channels involve high-frequency (fast) backbone skeletal vibrational motions promoting rapid energy dissipation.⁵ These processes take place on time scales < 100 fs; thus, charge separation of neutral, singlet excitons must occur on comparable or faster time scales.^{6,7} Recent studies have demonstrated the importance of fullerene crystallites in facilitating ultrafast charge separation before polymer exciton relaxation takes place.⁸ This mechanism requires substantial coupling between high-energy singlet exciton states and charge-separated states,⁵ which is ultimately dictated by blend

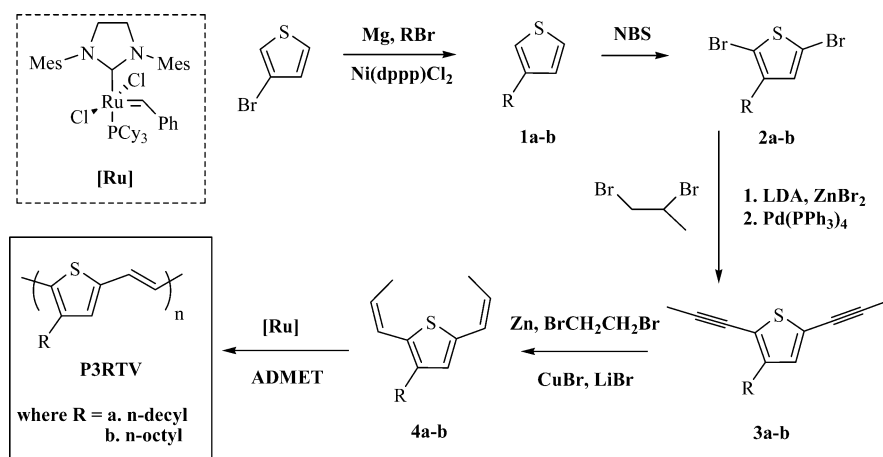
nanomorphology (e.g., polymer–fullerene miscibility and crystallinity). Charge separation yields may also be improved by extending the lifetimes of polymer excitons to ensure these bound states reach a fullerene interface before relaxing (radiatively or nonradiatively) back to the ground electronic state. This scenario is realized when singlet excitons spontaneously convert into spin-forbidden, triplet excitons with substantially longer lifetimes than their singlet counterparts.⁹ Singlet–triplet intersystem crossing is usually not efficient in conjugated organic molecules; however, singlet fission has received increased attention for splitting a singlet exciton into two triplets on ultrafast time scales.¹⁰ This process has been reported mostly in conjugated acenes, although recent studies have observed singlet fission in polythiophene systems.^{11,12} Interestingly, efficient singlet fission was demonstrated in dilute solutions of a poly(3-alkyl-thienylenevinylene)

Received: March 5, 2015

Published: April 1, 2015



Scheme 1. Synthesis Route of P3ATV



(P3ATV) derivative which has significant implications for potentially utilizing triplets before they relax back to the ground electronic state.¹¹ Harvesting triplet byproducts of singlet fission has also been proposed to increase charge generation yields,¹³ but it is less clear how singlet fission yields will be affected by the complex morphological landscape of photovoltaic polymer/fullerene blends in addition to the intrinsic conformational heterogeneity of polymers.

We use resonance Raman spectroscopy to study the extent of excited state geometric rearrangements and their dependence on the packing characteristics of two P3ATV molecules. Resonance Raman intensities are particularly sensitive to vibrations displaced in the initial allowed ¹B_u excited state and the local environment of the resonant chromophore. Previous photophysical studies of related P3ATV derivatives noted ultrafast relaxation to a low-lying dipole forbidden ²A_g excited state resulting in nearly quantitative fluorescence emission quenching.¹⁴ Musser et al. recently amended this interpretation by demonstrating that population of the ²A_g excited state in P3ATV solutions occurs from efficient intramolecular singlet fission on sub-100 fs time scales.¹¹ Although resonance Raman spectroscopy does not permit direct investigations of the ultrafast relaxation dynamics and optically forbidden (dark) excited states, it is possible to obtain detailed views of vibrational mode-specific geometrical displacements involving the initial “gateway” excited state in singlet fission. Moreover, excitation wavelength-dependent Raman frequencies and intensities reveal contributions from distinct structural forms that are usually masked in absorption spectra but nonetheless have a profound impact on photophysics and material performance.

P3ATV Raman spectra display well-resolved progressions of overtone and combination bands involving multiple high-frequency backbone symmetric stretching vibrations (~1200–1600 cm⁻¹) indicating a significantly distorted geometry change between the ¹A_g ground state and the ¹B_u excited state. Raman excitation profiles and frequency dispersion were next measured by varying laser excitation energy across the ¹A_g → ¹B_u absorption line shape that show larger enhancements near the red absorption edge and larger variation of Franck–Condon active P3ATV CC vibrational frequencies across the absorption envelope, respectively. We show these behaviors can be explained by excitation of aggregated and amorphous P3ATV chains with distinct optical and Raman line shapes. Similar behaviors have been reported in other polythiophene

systems, and this assignment is also supported by reports of polymorphism in related P3ATVs (i.e., two distinct P3ATV phases with different packing characteristics).¹⁵

Raman intensities were simulated by calculating the time-dependent Raman cross-correlation function for each displaced vibration that enabled estimates of mode-specific vibrational displacements in the excited state. These parameters were then used to simulate one-photon absorption spectra that showed excellent agreement with experimental P3ATV absorption spectra in the region where aggregates typically absorb. Subtracting simulated and experimental absorption spectra exposed a higher energy, weaker, and broadened absorption transition assigned to absorption of amorphous P3ATV chains. In a similar fashion, the characteristic Raman pattern of the amorphous component was elucidated by exciting P3ATV absorption spectra with *post*-resonant excitation and comparing to line shapes generated using *pre*-resonant excitation that preferentially selects only the aggregated component. The latter tend to dominate line shapes due to additional resonance enhancement effects, especially with longer (lower) wavelength (energy) excitation.

Functioning solar cell devices were next fabricated by blending P3ATVs with a soluble fullerene derivative to promote photoinduced charge transfer. Despite their lower energy absorption transitions and tendency to aggregate, P3ATVs have so far seen limited use in solar cells mainly owing to relatively poor power conversion efficiencies (PCE).^{16–19} Nonideal interface morphologies have been suggested as the chief origin of low PCEs and poor charge generation efficiency. However, detailed morphological studies and direct correlations to performance in device environments have been lacking. We apply our model to P3ATV solar cells using resonance Raman spectroscopic and photocurrent imaging to spatially map morphology-dependent structure to material performance. In-situ maps of aggregated and amorphous P3ATV fractions were constructed revealing new microscopic views of polymer/fullerene interactions that can be directly correlated to local photocurrent yields. Unlike other aggregating polymers, addition of fullerenes does not disturb P3ATV aggregate amounts and packing characteristics. However, larger photocurrent production was observed in aggregated regions with greater fullerene content (i.e., lower P3ATV Raman intensities) than corresponding amorphous regions. Greater demixing was observed in the amorphous P3ATV fraction (i.e., higher

P3ATV Raman intensities), resulting in photocurrent decreases presumably due to poor charge generation yields.

Our results have exposed not only the underlying spectroscopic signatures of aggregated and amorphous P3ATV structures but also important details of the vibrational mode-specific geometrical rearrangements incurred in the allowed 1B_u excited state. The latter may help shed light on the roles of high-frequency displaced vibrations in mediating early excited state relaxation processes. The relative insensitivity of each P3ATV fraction to the addition of fullerenes indicates weak interactions with the polymer-conjugated backbones, although these acceptors are probably more miscible with alkyl side groups. We propose that careful choice of side group substitution may enable reliable control of P3ATV packing and more favorable interactions with fullerenes to tune photo-physics as well as device performance.

■ EXPERIMENTAL SECTION

Synthesis. P3ATV derivatives were synthesized using the following procedure outlined in Scheme 1. Compounds **1a–4a**, **1b–4b**, and P3DTV were prepared according to previously reported procedures.²⁰

Poly(3-octylthienylene vinylene) (P3OTV). To a solution of **4b** (500 mg, 1.80 mmol) in 1,2,4-trichlorobenzene (TCB, 1.0 mL, anhydrous grade) was added Grubbs II catalyst (G2, 10.0 mg, 11.8 μ mol) in 1 mL of TCB under N_2 atmosphere. Dynamic vacuum was then applied, under which the resulting mixture was slowly heated to 90 $^{\circ}C$ and refluxed for 16 h. The reaction mixture was then cooled to rt and backfilled with N_2 , and 10 mg of G2 in 1 mL of TCB was added through a syringe. Dynamic vacuum was then reapplied, and the mixture was heated under reflux at 90 $^{\circ}C$ for another 16 h. The same procedure was applied after 16 h again. The solution was then diluted with a few milliliters of $CHCl_3$, and P3OTV was recovered by precipitation into methanol and washed by acetone, THF, and $CHCl_3$ in a Soxhlet extractor. P3OTV was isolated as a black powder by precipitation of the $CHCl_3$ solution into methanol and dried under high vacuum (360 mg, 72%). 1H NMR (300.13 MHz, $CDCl_3$): δ (ppm) = 1.23–1.28, 7.09–7.11, 7.36–7.38. ^{13}C NMR (75.48 MHz, $CDCl_3$): δ (ppm) = 1.18, 14.3, 22.87, 28.53, 29.46, 29.87, 30.92, 32.10, 119.33, 120.91, 129.64, 136.30, 140.17, 136.30, 140.17, 142.22. SEC ($CHCl_3$, 1 mL/min): M_n = 32.8 kDa, M_w = 65.6 kDa, PDI = 1.9.

Instrumentation and Device Fabrication and Characterization. Optical absorption spectra of P3DTV and P3OTV solutions and thin films (5 mg/mL) were acquired using a Shimadzu UV-2500 or a Hitachi U 4100 spectrophotometer equipped with a liquid-nitrogen-cooled cryostat. X-ray diffraction measurements were carried out on a Rigaku Smartlab X-ray diffractometer equipped with a high-speed 1D silicon strip detector (D/teX) and Cu- α as the X-ray source. Resonance Raman spectra were acquired on a home-built laser scanning confocal microscopic spectrometer equipped with krypton ion and argon ion gas lasers described in detail previously.²¹ Raman excitation profiles were generated by comparing intensities with a nonabsorbing external standard (sapphire).²² Scattered excitation light was removed by Rayleigh rejection filters (Semrock) prior to entering the polychromator/CCD detector system (Andor Shamrock 303i w/EMCCD). Raman spectra of P3ATV derivatives were also measured using preresonant excitation (i.e., 780 nm light) with a dispersive spectrometer (Nicolet) and compared to Raman

line shapes generated under resonant excitation. All frequencies were calibrated using pen ray lamps with known spectral responses.

Model photovoltaic devices were fabricated inside a nitrogen-circulating glovebox equipped with a thermal evaporator system. To generate the device active layer, the pristine polymer solution was blended with a solution of [6,6]-phenyl- C_{61} -butyric acid methyl ester (PCBM) (Nano-C, 15 mg/mL) followed by spin coating onto rigorously cleaned ITO-coated glass coverslips (Metavac) coated with a hole transport layer of PEDOT–PSS (Baytron). Substrates coated with PEDOT–PSS were heated at ~ 130 $^{\circ}C$ for ~ 30 min to remove any residual water before depositing the polymer/fullerene blend layer. Aluminum was next deposited (100 nm) by thermal vacuum deposition ($\sim 10^{-7}$ – 10^{-8} Torr) to complete the device. Current–voltage (I – V) characterization of devices was carried out inside the glovebox both in the dark and under AM1.5 illumination. Resonance Raman spectroscopic and photocurrent imaging were performed on solar cells using the same microscope setup described previously.²¹ Photocurrents were detected by sinusoidally modulating laser excitation and using a lock-in amplifier (Stanford Research Systems SR830). Excitation power densities were ~ 100 – 1000 W/cm 2 , and devices were placed in a home-built gas flow cell to avoid oxygen- and water-induced degradation.

■ RESULTS AND DISCUSSION

Figure 1 shows optical absorption spectra of P3DTV and P3OTV in solution and thin films. Both samples show a

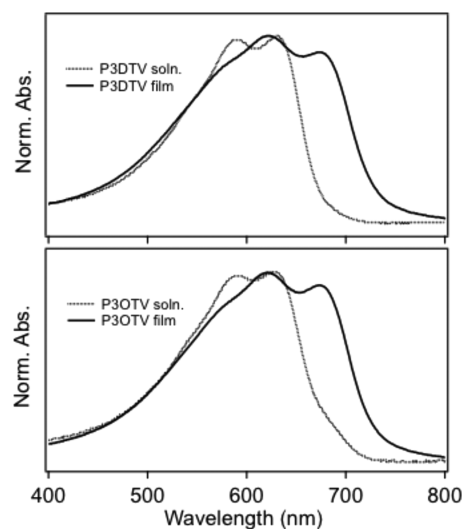


Figure 1. Absorption spectra of P3DTV (top) and P3OTV (bottom) solutions and thin films.

resolved vibronic progression interval of ~ 1450 cm^{-1} , and the lowest energy transition (i.e., electronic origin, 0–0) absorption strength varies significantly between solution and solid phases, but vibronic intervals are similar. The overall P3ATV absorption line shape profile closely resembles those from ordered (aggregating) polythiophenes.²³ The persistence of resolved vibronic structure in dilute solution suggests that P3ATV chains exist in collapsed conformations, which may correspond to aggregate seed precursors. This conformation is also consistent with observations of singlet fission in dilute solutions that require polymer chromophoric segments to be in

close proximity (i.e., significant interchain interactions) and possess suitable orientations.¹¹ In thin films, aggregates are more developed and exciton coupling is expected to be interchain in nature,¹⁵ similar to most polythiophenes,^{24,25} although packing distances differ from current benchmarks (e.g., regioregular poly(3-hexylthiophene) (P3HT)).

X-ray crystallography studies were next performed on P3ATV powders and thin films to further explore the nature of chain packing in aggregates. XRD data are shown in Figure 2

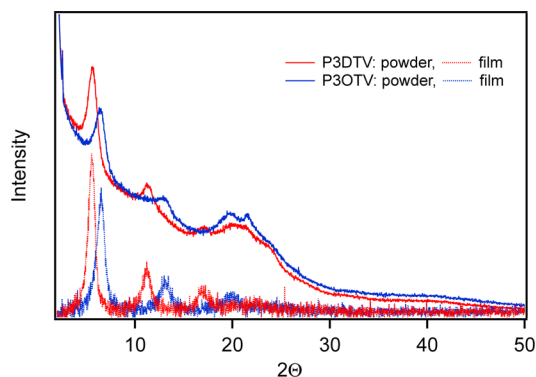


Figure 2. Powder and thin film XRD spectra of P3OTV and P3DTV.

for powders and thin films of P3DTV and P3OTV. Both P3ATV derivatives have similar patterns in both powder and thin film forms. Three scattering peaks positioned at 2θ values of 5.4° , 10.9° , and 16.4° are observed for P3DTV, corresponding, respectively, to the lamellar (100), (200), and (300) scattering and a d spacing of ca. 16.4 Å. This lamellar spacing is comparable with those reported for P3HT and shorter than the end-to-end distances of two stretched n -decyl groups, thus indicating intercalation of the side chains in the solid state. Similarly, three lamellar peaks at 2θ of 6.3° (100), 12.8° (200), and 19.3° (300) are observed for P3OTV, corresponding to a d spacing of ca. 14 Å that indicates side-chain intercalation between adjacent polymer chains. A relatively sharp peak at 2θ of 21.3° is also observed for the P3OTV powder, corresponding to a d spacing of ca. 4.2 Å. We tentatively assign this scattering peak to originate from π - π stacking, which is larger than that observed for P3HT ($d_{\pi-\pi}$ = 3.7 Å). This increase is presumably caused by the intercalation of the alkyl side chains and/or more backbone flexibility imparted by the main-chain double bonds.

Comparing XRD results with absorption trends in Figure 1 points to a large aggregated fraction in both P3ATV derivatives that dominates the overall absorption line shape. The slightly larger interlamellar spacings in P3DTV do not appear to significantly impact exciton characteristics compared to P3OTV. Absorption line shapes also appear qualitatively similar to P3HT aggregates near the low-energy onset region, but the larger π - π stacking distances suggest weaker exciton couplings than found in P3HT. Despite the prevalence of aggregates in absorption spectra and X-ray data, intrinsic polydispersity effects usually dictate that not all polymer chains adopt the same ordered conformations, leading to polymorphs as well as minority fractions of amorphous (unaggregated) chains. Spectroscopic contributions of unaggregated chains are typically broadened and blue-shifted transitions, and their relative amounts are usually strongly dependent on processing conditions.²³ A key goal of our study is to identify

spectroscopic contributions of underlying P3ATV aggregate and amorphous components and determine how these distinct structures affect material performance in device environments with complex morphologies. Furthermore, we will examine the extent to which specific vibrational modes couple to excitations and displace in the initial excited relative to their ground state equilibrium ground state geometry.

While useful, absorptive spectroscopies offer relatively limited views of aggregation, polymorphism, and excited state vibrational rearrangements mostly due to inhomogeneous broadening effects leading to line shapes with poorly resolved vibronic features. We instead turn to resonance Raman spectroscopy to examine Franck–Condon active vibrations by selectively exciting across the allowed $^1A_g \rightarrow ^1B_u$ absorption transition line shape (Figure 1). Resonance excitation often produces large enhancements of Raman-active modes displaced in the excited state, and intensities are sensitive to the local environment of the chromophore. These features, along with sharp spectral line widths, make resonance Raman spectroscopy ideal for unmasking contributions from distinct structural subspecies that are usually masked by overlapping and broadened transitions in absorption spectra.

Figure 3a shows representative resonance Raman spectra of P3DTV thin films excited with 488 nm light corresponding to

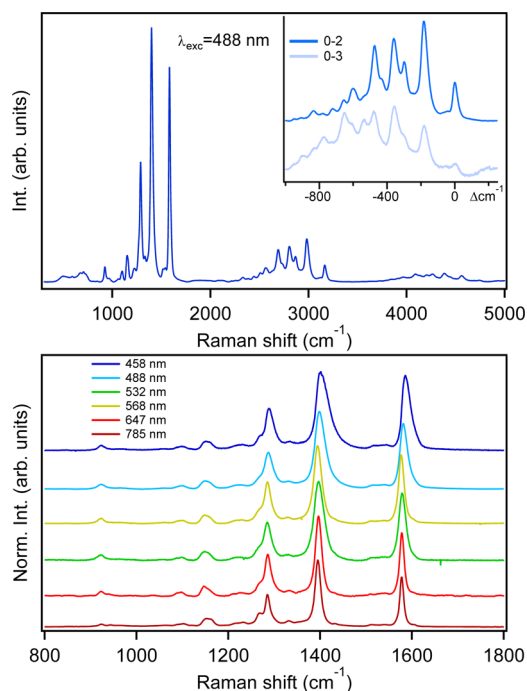


Figure 3. Resonance Raman spectrum of P3DTV (λ_{exc} = 488 nm) showing multiple resolved progressions of overtone and combination bands (top). Comparison of Raman line shapes as a function of excitation wavelength (bottom).

the high-energy tail of the absorption spectrum. Raman line shapes of both P3ATV derivatives were virtually identical, similar to one-photon absorption spectra (Figure 1), confirming the similar nature of chromophore segments despite minor variations in packing distances. Multiple overtone/combination band progressions are resolved involving the C–C and C=C symmetric stretching vibrations of the P3DTV backbone (see Table 1). These features indicate a significantly distorted excited state geometry along multiple vibrational

Table 1. Experimental P3ATV Raman Vibrational Modes and Assignments and Calculated Displacements

mode (<i>k</i>)	frequency (cm ⁻¹)	Δ_k (dimensionless) ^a	assignment ^b
ν_1	562	0.54	
ν_2	664	0.21	thienylene ring C–H wag
ν_3	913	0.27	vinyl C–H out-of-plane wag
ν_4	953	0.27	vinyl bend
ν_5	1047	0.2	thienylene C–H bend
ν_6	1088	0.2	inter-ring C–C breathing modes
ν_7	1143	0.51	
ν_8	1210	0.24	
ν_9	1278	0.67	vinyl C–H bend
ν_{10}	1390	0.87	thienylene ring C=C stretch
ν_{11}	1573	0.67	vinyl C=C stretch
first overtone/combination region			
$\nu_3 + \nu_{10}$	2315		
$\nu_7 + \nu_9$	2430		
$\nu_6 + \nu_{10}$	2490		
$2\nu_9$	2555		
$\nu_9 + \nu_{10}$	2680		
$2\nu_{10}$	2790		
$\nu_9 + \nu_{11}$	2855		
$\nu_{10} + \nu_{11}$	2970		
$2\nu_{11}$	3155		

^aFrom time-dependent simulations of the Raman cross-correlation overlap function. $\Gamma = 380 \text{ cm}^{-1}$; $E_{0-0} = 14\,700 \text{ cm}^{-1}$. ^bReference 37.

coordinates. We next evaluated the effect of excitation wavelength (energy) on the Raman line shapes, and Figure 3b displays the fundamental region of P3DTV thin films. As excitation wavelengths decrease, line widths broaden on the blue edge of the prominent, higher frequency thienylene and vinylene C=C stretching modes (1390 cm^{-1} , ν_{10} , and 1573 cm^{-1} , ν_{11}) and apparent blue shifts of frequencies up to $\sim 15 \text{ cm}^{-1}$ were observed. P3ATV Raman spectra were next measured with 780 nm light, which is preresonant with the main absorption line shape (Figure 1) and should interrogate only longer chromophore segments. Comparison of pre- and postresonant Raman line shapes (e.g., 780 vs 458 nm excitation) reveals stark differences in line widths, frequencies, and intensities, although patterns are similar, i.e., overtone/combination transitions are still resolved with preresonant excitation and no new transitions are present. This indicates resonance enhancements are derived solely from the allowed 1B_u excited state,^{26,27} but the large variation in line widths and frequencies is suggestive of selective excitation of structurally distinct P3ATV chains with different absorptivity coefficients and concentrations. We reported similar behavior in well-studied polythiophenes and polythienophenes where Raman signatures vary strongly with choice of excitation wavelength and material processing conditions.²⁸ Previous spectroscopic and theoretical studies of a related P3ATV derivative also noted the presence of two distinct geometrical phases differing in interchain stacking distance.¹⁵

In addition, the near quantitative fluorescence quenching in P3ATVs by rapid relaxation to the dark 2A_g excited state may have implications for Raman scattering when excitation is resonant with the allowed 1B_u state. For example, Ozaki et al. observed larger frequency dispersion for P3ATVs compared to common light-emitting polymers and attributed this behavior to the presence of A_g excited states in close proximity with

allowed 1B_u states.²⁶ Unfortunately, it is not possible to directly probe these states with Raman, and attempts to measure their absorption spectra (e.g., by increasing sample concentrations) proved ineffective (see Supporting Information). To help sort out contributions from either conformational polymorphs or dark excited states, we examine excitation wavelength-dependent Raman intensities and frequencies. Raman frequency dispersion plots for both P3ATV derivatives were generated using the method described in ref 26 that takes the product of the squares of scaled frequencies. We consider only the dominant progression forming P3ATV backbone vibrations (ν_{9-11}), and plots were scaled using the frequencies obtained from preresonance excitation, ω_0 (i.e., 780 nm excitation), corresponding to excitation of the lowest energy chromophores (longest conjugation length). Frequency dispersion plots are shown in Figure 5, and comparisons to previously published results from related P3ATV derivatives measured over the same excitation wavelength (energy) range reveal similar trends.²⁶

In addition to excitation dependent vibrational frequencies, Raman excitation profiles measure the intensity of a specific band as a function of excitation wavelength and are capable of exposing underlying excited states contributing to Raman scattering. In the case of overlapping and couple excited states, Raman profiles usually exhibit anomalous behavior (e.g., de-enhancements) from interference effects.^{29,30} These may be apparent from comparisons with absorption spectra in the form of dips or nonconstant vibronic intervals and non-Poissonian envelopes. Figure 6 shows experimental resonance excitation profiles of P3DTV for the ν_9 – ν_{11} fundamental and overtone transitions generated by using an external intensity standard (sapphire). P3OTV excitation profiles show nearly identical behavior and are included in the Supporting Information. Herein we display representative spectroscopic data for either P3ATV derivative for brevity due to their nearly identical features and behavior.

Relative Raman cross sections of ν_9 – ν_{11} fundamentals are smaller for shorter excitation wavelengths and then increase substantially at longer excitation wavelengths. Raman first-overtone profiles show similar patterns across the P3ATV main absorption envelope but deviate from fundamental profiles probably from their different time evolution characteristics.^{31,32} Enhanced activity near the red absorption edge is apparent and suggests either enhanced contributions from aggregates, consistent with the weakly resolved vibronic features in the low-energy region of the absorption spectrum (Figure 1) or possibly interference from dark (A_g) excited states on the high-energy absorption tail. Similar Raman enhancements from π -stacked polymer aggregates have been demonstrated in P3HT and confirmed by varying processing conditions (i.e., aggregate content).³³ McHale and co-workers also reported detailed resonance Raman data from molecular nanoaggregates and described a secondary resonance enhancement effect from these structures.³⁴

Excitation wavelength-dependent Raman intensities and frequency dispersion behavior in Figures 4 and 5 are characteristic of selective excitation of structurally distinct P3ATV chains as opposed to previously proposed interactions with dark excited states. In this picture, aggregated P3ATV chains absorb in the lower energy (longer wavelength) region and, based on absorption and X-ray data, represent the dominant structural form in thin films. Conversely, amorphous (unaggregated) chains tend to absorb at higher energies (shorter wavelength) and correspond to minority species with

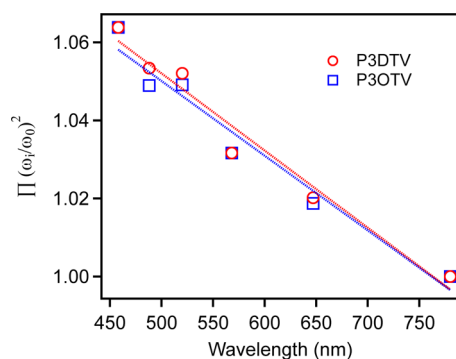


Figure 4. Raman dispersion plots for P3DTV and P3OTV thin films.

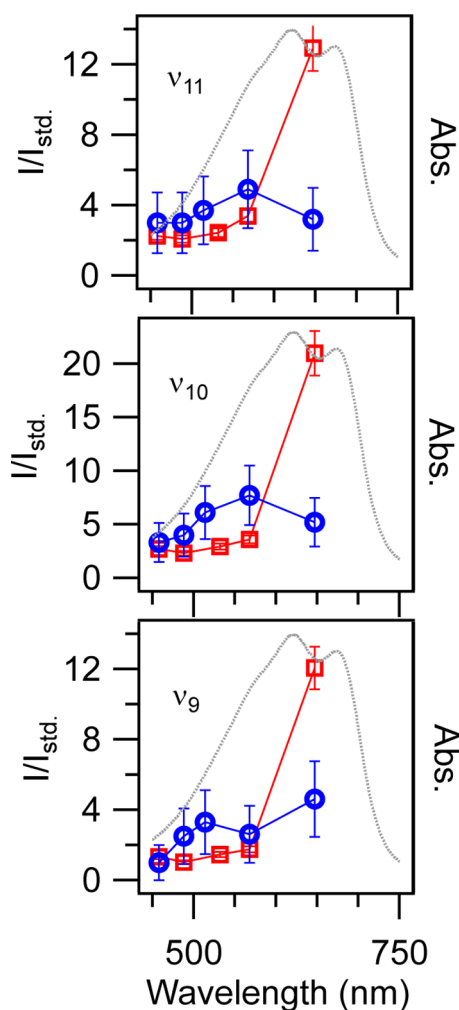


Figure 5. Raman excitation profiles for P3OTV thin film main skeletal vibrations (ν_9 – ν_{11}). Fundamentals (0–1, red open squares) and first overtones (0–2, blue open circles) are shown. Thin film absorption spectra are shown for comparison.

shorter conjugated segments due to disorder. Discerning spectral line shapes of P3ATV structures can be accomplished by analyzing Raman line shapes generated on resonance with electronic absorption transitions from either structural form. We now use time-dependent wavepacket simulations to calculate Raman intensities and absorption spectra that, in addition to extracting mode-specific excited state geometrical rearrangements, provide a basis for discerning line shape contributions from aggregated and amorphous P3ATV chains.

Time-Dependent Raman Intensity and Absorption Simulations.

We first calculate the time-dependent Raman cross-correlation function for each displaced P3ATV vibrational mode using the framework developed by Heller and co-workers.^{31,32} The model assumes that both ground and excited electronic states are undistorted harmonic potentials, and the transition dipole is not dependent on vibrational coordinates. In this limit, the cross-correlation overlap function can be calculated analytically for fundamentals and overtones as well as combination band transitions involving up to 3 modes. The total time-dependent overlap is given in eq 1, which is the product of overlaps from each displaced mode.

$$\langle \phi_f | \phi(t) \rangle = \prod_k \left\{ \exp \left[-\frac{\Delta_k^2}{2} (1 - \exp(-i\omega_k t)) - \frac{i\omega_k t}{2} \right] \right. \\ \times \dots \\ \left. (1 - \exp(-i\omega_k t))^{n_k} \times \frac{(-1)^{n_k} \Delta_k^{n_k}}{(2^{n_k} n_k!)^{1/2}} \right\} \quad (1)$$

The parameters Δ_k and n_k are the displacement and order of the k th vibrational mode. The Raman polarizability, α , and intensities are obtained by a half Fourier transform of the cross-correlation overlap

$$[\alpha_{fi}] = \frac{i}{\hbar} \int_0^\infty \langle \phi_f | \phi(t) \rangle \times \exp\{i(\omega_k + \omega_l)t\} \\ - (E_{0-0} + \Gamma)t\} dt \quad (2)$$

$$I_{i-f} \propto \omega_l \omega_k^3 [\alpha_{fi}]^* [\alpha_{fi}] \quad (3)$$

The zero-point vibrational frequencies, ω_k , and energy of the electronic origin, E_{0-0} are obtained directly from experimental Raman and absorption spectra and held constant. The fitting procedure entails adjusting vibrational displacements, Δ_k , at a constant incident excitation frequency, ω_p , until good agreement between experimental and calculated intensities is obtained. Γ is a phenomenological damping factor that attenuates the overlap amplitude and, when excited on resonance, represents the characteristic lifetime of the chromophore (including coupling to the surrounding medium). In the following we briefly discuss the physical implications of these parameters, and additional details of the model can be found in refs 31 and 32.

Figure 6a shows simulated Raman intensities from the time-dependent wavepacket model and experiment, and best-fit parameter values are listed in Table 1. Overall, the fits reproduce relative experimental intensities including overtones and combination bands. It is interesting to note that several weak combination bands involving lower frequency backbone bending vibrations appear in the vicinity of the dominant CC stretches, similar to experiment. The good correspondence between theory and experiment indicates that the actual potential energy surfaces are not significantly distorted from the ideal harmonic oscillator approximation used here.

We now use the same parameters to simulate the one-photon absorption spectrum (Figure 6b), which not only serves as an independent check on fitted parameters (i.e., Δ_k and Γ) but also reveals potential contributions from other states and structural forms. The simulated absorption spectrum exhibits a weakly resolved vibronic progression similar to experiment with excellent agreement near the band maximum and low-energy

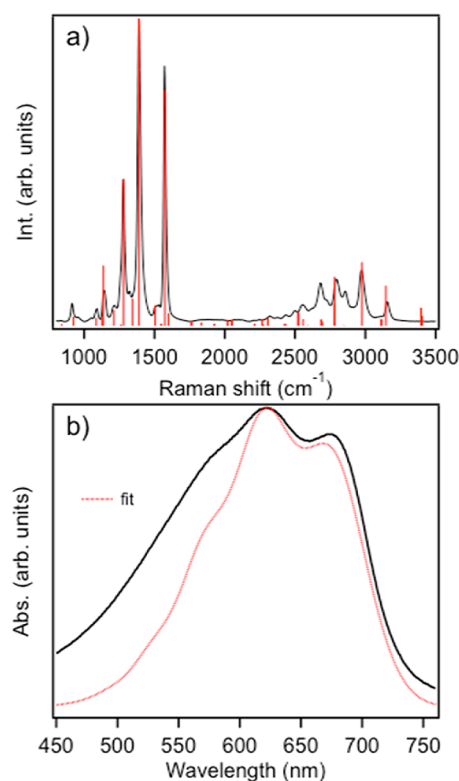


Figure 6. (a) Comparison of simulated (red sticks) and experimental (black) P3ATV Raman intensities ($\lambda_{\text{exc}} = 488$ nm). Fit parameters are provided in Table 1. (b) Simulated (red dotted trace) and experimental (black solid trace) absorption spectra.

onset. We assign this region as absorption of P3ATV aggregates. The discrepancy between the fit and the high-energy tail of the experimental absorption spectrum is—based on our earlier studies with P3HT—indicative of absorption contributions from shorter, less-ordered (unaggregated) P3ATV segments that represent the amorphous fraction. Importantly, contributions from exciton coupling are neglected in our approach, although these values are expected to be considerably smaller than the benchmark P3HT system due to larger π -stacking distances in P3ATV aggregates. This is supported by the fact that absorption fit parameters were obtained independently from Raman intensity simulations, meaning that exciton coupling contributions would probably not lead to appreciable changes in the absorption vibronic line shape beyond the harmonic approximation.

It is also possible to simulate Raman excitation profiles using eqs 1–3 by varying the incident photon energy (ω_i) for each mode while holding all other fit parameters constant. Simulated profiles are included in the Supporting Information and show similar qualitative characteristics as experimental profiles (i.e., enhancements near the absorption maximum and low-energy onset). More detailed comparisons between experimental and calculated profiles were not possible because of the lack of sufficient excitation wavelengths near the P3ATV absorption onset and maximum.

In addition to exposing vibrational mode-specific excited state rearrangements in P3ATV aggregates, it is informative to consider the implications of Γ that dictate the extent to which time-dependent vibrational wavepackets propagate on the excited state potential surface. Although this parameter is described here as a phenomenological damping term, it

represents the intrinsic lifetime of the resonant chromophore and coupling to the medium (e.g., phonon bath). Comparing mode-specific wavepacket cross-correlation overlaps (see Supporting Information) reveals that the high-frequency P3ATV backbone vibrations (i.e., ν_{9-11}) make at least two return visits to the Franck–Condon region before their amplitude is completely damped. This feature can also be understood by comparing vibrational periods given by $(c\hbar\omega)^{-1}$, where c is the speed of light and $\hbar\omega$ is the vibrational frequency in cm^{-1} , with the characteristic time of Γ . From this relationship, the periods of ν_{9-11} are in the range of ~ 20 – 30 fs, much smaller than Γ (~ 90 fs). Interestingly, characteristic time scales of singlet fission from the initial $^1\text{B}_u$ excited state were reported to be ~ 45 fs.^{11,14} The survival of the ν_{9-11} Raman wavepacket for several periods on the $^1\text{B}_u$ state potential surface suggests that electronic relaxation processes on similar time scales are possibly coupled to displaced backbone vibrational motions. This result uncovers potentially vital roles of vibrations in mediating relaxation between excited states beyond what is currently understood from pure electronic energy level models borne out from dynamics studies that neglect vibrations.¹¹ Furthermore, aggregated and amorphous P3ATV chains should have markedly different relaxation characteristics and singlet fission yields due to different exciton coherence lengths and singlet–triplet energy splitting. However, the overlapping nature of these absorption transitions in addition to spectral resolution limits of transient absorption techniques mask these contributions. It is important to stress that while we are not directly measuring relaxation dynamics between different excited electronic states, these processes must be considered as vibration assisted and we expect that time-resolved Raman experiments may further uncover details of the extent of vibrational coupling in interstate relaxation processes (i.e., Franck–Condon factors).

Thus far we uncovered two new and important results that advance our understanding of P3ATV structural and electronic properties: (i) excited state geometries are significantly distorted along multiple coordinates relative to the ground electronic state unlike well-studied P3HT aggregates;³³ (ii) it is now possible to decompose experimental spectroscopic line shapes into contributions from both aggregated and amorphous P3ATV chains.

The absorption signatures of amorphous P3ATV fractions can now be visualized by subtracting the simulated absorption spectrum from experiment (Figure 6b). Figure 7a shows experimental and simulated P3ATV absorption spectra and difference spectra. A Gaussian function is fitted to the latter to determine line width and λ_{max} . As expected, these P3ATV absorb at higher energy, and line shapes are nearly devoid of resolved vibronic structure. Raman spectra of aggregated and amorphous P3ATV forms are obtained from selective excitation of their distinct absorption line shapes in Figure 7a. P3ATV aggregate Raman signatures are generated by exciting on the red edge of the aggregate absorption (780 nm), whereas the amorphous form is selected using 458 nm light (Figure 7b). Absorption cross-talk is likely in the latter excitation regime due to small, but nonzero, absorption of the aggregates. As shown in Figure 7, both Raman line shapes have different characteristic frequency maxima and relative intensity distributions that can now serve as markers for determining the relative amounts of each species and variations in their structural properties. We chose not to fit the amorphous P3ATV absorption line shape

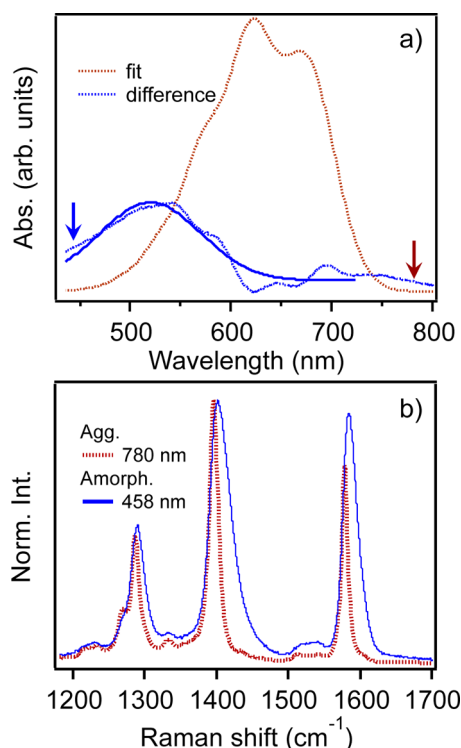


Figure 7. (a) Simulated P3ATV absorption and difference spectra generated from subtraction of the fit from the experimental line shape. A Gaussian function was fitted to the difference spectrum to extract band maxima wavelengths. (b) Raman signatures of the limiting aggregated (red) and amorphous (blue) P3ATV forms generated by selective resonance excitation (denoted by downward arrows in a).

due to the lack of resolved structure that may lead to large uncertainty in fit parameters (i.e., Δ and Γ).

Resonance Raman and Photocurrent Imaging of P3ATV Solar Cells. The crystalline nature and lower energy absorption of P3ATVs make them good candidates for solar cell applications due to the prospect of enhanced charge transport and better harvesting of NIR solar photons. However, these materials have not performed nearly as well as related polythiophenes, which is believed to stem from nonideal morphologies when blended with suitable electron acceptors (e.g., soluble fullerenes). These shortcomings may possibly be alleviated if triplet excitons can be harvested following singlet fission to generate multiple charges with a single photon. Unfortunately, basic structure–property knowledge has lagged considerably behind, thus limiting rational design strategies to optimize material performance. We now extend our studies to mapping microscopic structure–function relationships in model P3ATV/fullerene solar cells using resonance Raman and photocurrent imaging techniques. This approach benefits from our ability to resolve contributions from both aggregated and amorphous P3ATV fractions that are sensitive to changes in local packing and composition (i.e., fullerene content).

Bulk heterojunction (BHJ) type solar cells are fabricated by blending P3ATVs with a soluble fullerene derivative, PCBM, in solution and then spin cast to form the active layer. As previously shown in other polymer/fullerene blends, the polymer aggregate fraction is usually diminished when fullerenes are added but can be partially restored by annealing.³⁵ We exploit the high sensitivity of resonance Raman intensities to the polymer packing characteristics and

generate in-situ maps of how specific structural variants are affected by local film composition (morphology). Moreover, valuable correlations between microscopic structure and performance are exposed that are not obtainable by conventional ensemble device and spectroscopic characterization or electromechanical surface probe techniques.

Figure 8 shows I – V curves of P3ATV solar cells in the dark and under AM1.5 irradiation for as-cast films. Overall, PCEs

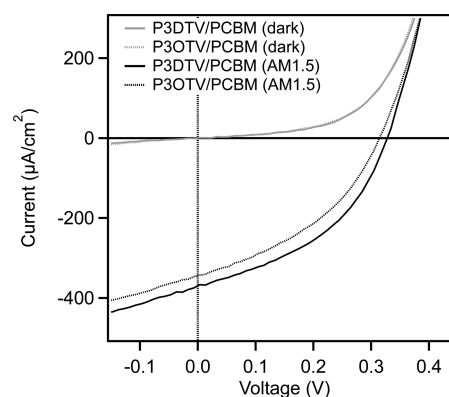


Figure 8. I – V curves of model P3ATV/PCBM solar cells in the dark and under AM1.5 illumination.

were typically <1%, similar to previous results from similar P3ATV/fullerene blends.¹⁹ Light thermal annealing treatments (e.g., 130 °C, 20–30 min) brought about small improvements in performance, and small (<1 μ m) fractal-like crystallites of PCBM became apparent in films annealed for longer times. Open-circuit voltages (V_{OC}) are \sim 0.28–0.32 V, smaller than those found in more common polythiophene derivatives, consistent with either smaller HOMO–LUMO (donor–acceptor) energy offsets or unfavorable interface morphologies.³⁶

Resonance Raman and photocurrent imaging of P3ATV/PCBM solar cells was performed using an approach described in detail earlier.²¹ The 532 nm line of a Kr-ion laser served as the excitation source that excites both aggregated and amorphous P3ATV components nearly equally, and the device was raster scanned over the diffraction-limited laser spot to generate Raman and photocurrent images over the same scan area. Excitation intensities were \sim 1 kW/cm² for both measurements, which was necessary to produce currents above the detection limit due to the intrinsically low PCE. Figure 9 shows resonance Raman and photocurrent images for a representative annealed P3DTV/PCBM device. Raman images are produced by mapping the integrated intensity for a particular band, and we focus on the dominant P3DTV C=C thiophene- and vinyl-symmetric stretches ($\nu_{10,11}$) displayed in Figure 9a and 9b. Corresponding photocurrent images for the same scan are shown in Figure 9c. As-cast devices showed little discernible phase separation in both Raman and photocurrent images (see Supporting Information), indicating a well-mixed phase or separation below the spatial resolution of the instrument.

Comparing photocurrent and Raman intensity images for annealed devices reveals decreases in current production in regions with larger P3DTV concentration (intensity). This feature originates from some demixing between the polymer and the fullerene leading to poor charge generation. Surrounding regions show improved photocurrent production,

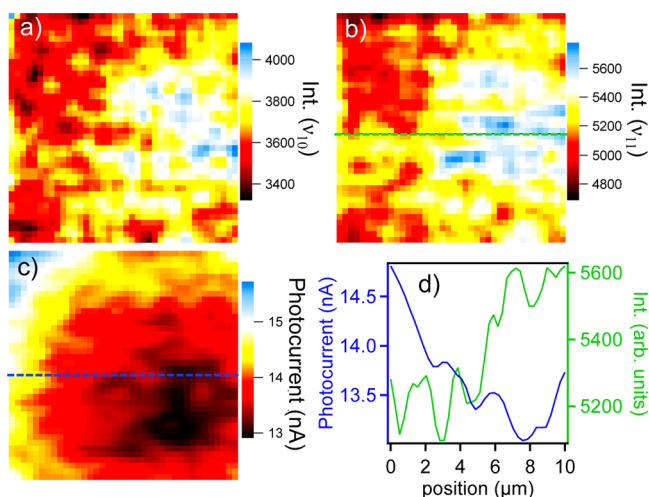


Figure 9. Raman and photocurrent images of an annealed P3DTV/PCBM solar cell under 532 nm excitation. Integrated intensity images (a, b) of C=C thienylene (ν_{10}) and vinylene (ν_{11}) stretches. Photocurrent magnitude (c) from the same scan area ($10 \times 10 \mu\text{m}$), and (d) comparison of Raman intensity and photocurrent line scans denoted in b and c.

suggesting better mixing and charge separation efficiency. Similar observations have been noted in annealed P3HT/PCBM blends where current decreases are observed in PCBM crystallites and P3HT aggregates due to the inability of PCBM to intercalate in the latter structures. Line scans of the ν_{11} mode Raman intensity image and photocurrent for the same region (Figure 9d) further illustrate the anticorrelation between P3ATV-rich regions and photocurrent generation efficiency. Again, these aspects are qualitatively similar to P3HT/PCBM solar cells where the tendency of both components to crystallize negatively impacts charge generation yields because of phase segregation when films are annealed. However, the miscibility characteristics of PCBM in P3ATVs are expected to differ considerably owing to the additional vinylene linkage between thiophene groups as well as longer alkyl side groups and packing distances. Previous X-ray scattering studies of a related P3ATV blended with PCBM revealed that both components were well mixed in the regime of 1:1 w/w loadings or less.¹⁹ Moreover, P3ATV aggregate diffraction peaks are still present and unaltered from the pristine state in this PCBM loading range.¹⁹ This was further confirmed by measuring absorption spectra of P3ATV/PCBM blends that showed no significant changes in the P3ATV absorption line shape implying that PCBM mixes well with both polymer forms (see Supporting Information). Additionally, Raman spectra of P3ATV/PCBM blends (1:1 w/w) were measured with 780 nm light to verify the nature of aggregate chain packing and found virtually identical line shapes compared to pristine P3ATVs excited at the same wavelength (see Supporting Information).

Using our multispecies description of P3ATV optical and Raman spectra, it is now possible to spatially map contributions from aggregated and amorphous fractions of P3ATV in the blend solar cell active layer. We use Raman spectra of the two limiting forms identified earlier in Figure 7 and perform a linear least-squares fit of experimental Raman line shapes used to construct intensity images in Figure 9. Figure 10 shows integrated intensities of aggregated (Figure 10a and 10b) and amorphous (Figure 10c and 10d) P3ATV chains for ν_{10} and ν_{11} modes, respectively. Distinct correlations between the locations

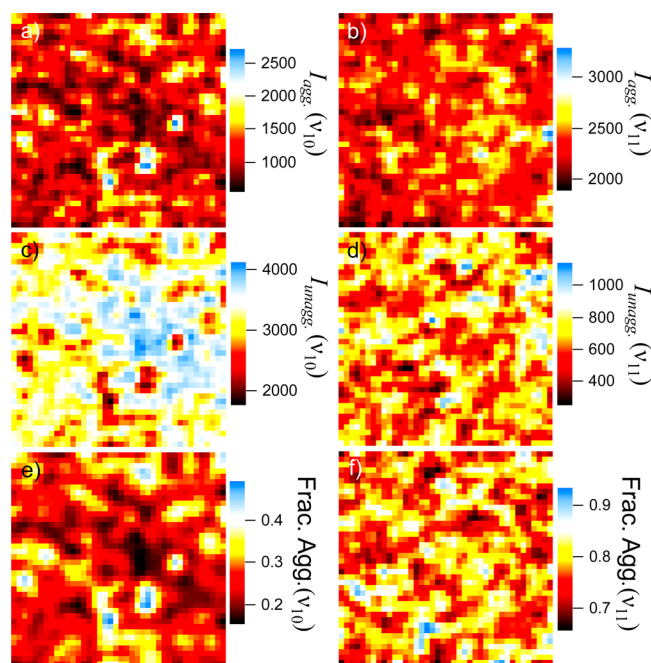


Figure 10. Raman integrated intensity images of modes ν_{10} and ν_{11} for aggregated (a, b) and unaggregated (c, d) P3ATV components. (e and f) Images of the aggregated fractions.

of aggregated and amorphous chains are apparent in ν_{10} images involving the thienylene-symmetric C=C stretching, and the results clearly show regions with greater amorphous fractions correspond to lower photocurrent output. This behavior is opposite of that observed in P3HT/PCBM where crystallization causes currents to decrease in aggregated regions. It is also important to note that the size scale and shapes of domain features are also different, which most likely originates from the molecular miscibility of PCBM with P3ATV.

On the basis of the invariance of absorption and Raman line shapes upon addition of PCBM, we propose that fullerenes remain on the periphery of P3ATV chains (either aggregates or amorphous) and do not interact significantly with the backbone. This is consistent with X-ray scattering studies showing that phase separation does not occur until PCBM loadings exceed 1:1 w/w, suggesting PCBM molecules tend to remain in P3ATV alkyl side groups or at domain boundaries.¹⁹ Furthermore, no change in aggregate π -stacking or interlamellar spacing was observed when PCBM was added, which is consistent with the insensitivity of excitons to minor disturbances involving side groups. The reduced PCBM amounts in amorphous P3ATV zones is surprising generally because these chains can more readily accommodate fullerenes compared to aggregates where close packing can restrict access. This behavior indicates that PCBM may stabilize aggregates or possibly induce aggregation and ordering. However, annealing promotes PCBM crystallization, which might destabilize aggregates. Although we are pursuing detailed studies to further understand this phenomenon, the overall weaker interaction between P3ATVs and fullerenes elucidated from Raman spectroscopy and imaging helps close the loop in explaining the molecular origins of poor performance in solar cells.

CONCLUSIONS

We used CW resonance Raman probes of nonemissive P3ATV systems to expose vibrational mode-specific excited state structural displacements and contributions of intrinsic polymorphs that have so far gone unreported in this class of polymers. X-ray diffraction and optical absorption spectroscopy verified the preponderance of aggregate formation in P3ATVs that remains undisturbed even in the presence of appreciable amounts of fullerenes. Excitation wavelength-dependent Raman frequencies and intensities showed strong evidence for overlapping transitions from both aggregated and amorphous P3ATV chains. This assignment was confirmed by time-dependent Raman wavepacket simulations to calculate Raman intensities, and parameters were then used to generate absorption spectra that showed excellent agreement with experiment. Simulated absorption spectra were subtracted from experiment to reveal the line shape of the minority amorphous P3ATV fraction. Raman line shapes of each P3ATV structural form were generated by selective resonance excitation of their characteristic absorption line shapes. This new description of distinct structural variants in P3ATV derivatives explains all observed spectroscopic behaviors without the need to invoke contributions of optically forbidden A_g dark states.

By extending this model to resonance Raman and photocurrent imaging studies of P3ATV/PCBM blend solar cells, we further uncovered new structure–function correlations. For example, spatial maps of morphology-dependent distributions of the limiting aggregated and amorphous P3ATV forms were produced and directly correlated with photocurrent production in the same scan area. Interestingly, regions with larger aggregate fractions showed larger photocurrents, contrary to earlier findings in the benchmark P3HT/PCBM blend, indicating better mixing with fullerenes. On the other hand, P3ATV-rich regions correspond to the amorphous fraction that have lower photocurrent output. Overall, these results confirm that although PCBM mixes well with both fractions the length of separation between polymer donors and fullerene acceptors is significantly larger than in related polymers. We believe this may be due to P3ATV side groups or chain packing arrangements (i.e., interpenetrating side groups), restricting PCBM from interacting with the conjugated backbone segments. The invariance of absorption, X-ray, and Raman spectra of P3ATV aggregates in the presence of PCBM support this hypothesis, which explains overall poor charge generation yields in these materials. We expect that new strategies to tune side group substitution patterns may enable better mixing and improve material performance.

ASSOCIATED CONTENT

Supporting Information

NIR absorption spectra of P3ATV thin films, experimental and calculated Raman excitation profiles, calculated Raman cross-correlation overlaps, Raman and photocurrent images of P3DTV/PCBM solar cells, absorption and Raman spectra of P3ATV/PCBM blends. This material is available free of charge via the Internet at <http://pubs.acs.org>.

AUTHOR INFORMATION

Corresponding Author

*E-mail: jkgrey@unm.edu.

Notes

The authors declare no competing financial interest.

ACKNOWLEDGMENTS

J.K.G. acknowledges financial support from the National Science Foundation (CHE-0955242).

REFERENCES

- (1) Thompson, B. C.; Frechet, J. M. J. Polymer-Fullerene Composite Solar Cells. *Angew. Chem., Int. Ed.* **2008**, *47*, 58–77.
- (2) Clarke, T. M.; Durrant, J. R. Charge Photogeneration in Organic Solar Cells. *Chem. Rev.* **2010**, *110*, 6736–6767.
- (3) Coakley, K. M.; McGehee, M. D. Conjugated Polymer Photovoltaic Cells. *Chem. Mater.* **2004**, *16*, 4533–4542.
- (4) Bredas, J.-L.; Durrant, J. R. Organic Photovoltaics. *Acc. Chem. Res.* **2009**, *42*, 1689–1690.
- (5) Grancini, G.; Maiuri, M.; Fazzi, D.; Petrozza, A.; Egelhaaf, H. J.; Brida, D.; Cerullo, G.; Lanzani, G. Hot Exciton Dissociation in Polymer Solar Cells. *Nat. Mater.* **2013**, *12*, 29–33.
- (6) Muller, J. G.; Lupton, J. M.; Feldmann, J.; Lemmer, U.; Scharber, M. C.; Sariciftci, N. S.; Brabec, C. J.; Scherf, U. Ultrafast Dynamics of Charge Carrier Photogeneration and Geminate Recombination in Conjugated Polymer:Fullerene Solar Cells. *Phys. Rev. B* **2005**, *72*, 195208/1–195208/10.
- (7) Lanzani, G.; Cerullo, G.; Polli, D.; Gambetta, A.; Zavelani-Rossi, M.; Gadermaier, C. Photophysics of Conjugated Polymers: The Contribution of Ultrafast Spectroscopy. *Phys. Status Solidi A* **2004**, *201*, 1116–1131.
- (8) Gelinas, S.; Rao, A.; Kumar, A.; Smith, S. L.; Chin, A. W.; Clark, J.; van der Poll, T. S.; Bazan, G. C.; Friend, R. H. Ultrafast Long-Range Charge Separation in Organic Semiconductor Photovoltaic Diodes. *Science* **2014**, *343*, 512–516.
- (9) Koehler, A.; Baessler, H. Triplet States in Organic Semiconductors. *Mater. Sci. Eng., R* **2009**, *R66*, 71–109.
- (10) Smith, M. B.; Michl, J. Singlet Fission. *Chem. Rev.* **2010**, *110*, 6891–6936.
- (11) Musser, A. J.; Al-Hashimi, M.; Maiuri, M.; Brida, D.; Heeney, M.; Cerullo, G.; Friend, R. H.; Clark, J. Activated Singlet Exciton Fission in a Semiconducting Polymer. *J. Am. Chem. Soc.* **2013**, *135*, 12747–12754.
- (12) Guo, J.; Ohkita, H.; Bente, H.; Ito, S. Near-Ir Femtosecond Transient Absorption Spectroscopy of Ultrafast Polaron and Triplet Exciton Formation in Polythiophene Films with Different Regio-regularities. *J. Am. Chem. Soc.* **2009**, *131*, 16869–16880.
- (13) Smith, M. B.; Michl, J. Recent Advances in Singlet Fission. *Annu. Rev. Phys. Chem.* **2013**, *64*, 361–386.
- (14) Olejnik, E.; Pandit, B.; Basel, T.; Lafalce, E.; Sheng, C. X.; Zhang, C.; Jiang, X.; Vardeny, Z. V. Ultrafast Optical Studies of Ordered Poly(3-Thienylene-Vinylene) Films. *Phys. Rev. B* **2012**, *85*, 235201/1–235201/6.
- (15) Gavrilenko, A. V.; Matos, T. D.; Bonner, C. E.; Sun, S. S.; Zhang, C.; Gavrilenko, V. I. Optical Absorption of Poly(Thienylene Vinylene)-Conjugated Polymers: Experiment and First Principle Theory. *J. Phys. Chem. C* **2008**, *112*, 7908–7912.
- (16) Smith, A. P.; Smith, R. R.; Taylor, B. E.; Durstock, M. F. An Investigation of Poly(Thienylene Vinylene) in Organic Photovoltaic Devices. *Chem. Mater.* **2004**, *16*, 4687–4692.
- (17) Henckens, A.; Knipper, M.; Polec, I.; Manca, J.; Lutsen, L.; Vanderzande, D. Poly(Thienylene Vinylene) Derivatives as Low Band Gap Polymers for Photovoltaic Applications. *Thin Solid Films* **2004**, *451–452*, 572–579.
- (18) Girotto, C.; Cheyng, D.; Aernouts, T.; Banishoeib, F.; Lutsen, L.; Cleij, T. J.; Vanderzande, D.; Genoe, J.; Poortmans, J.; Heremans, P. Bulk Heterojunction Organic Solar Cells Based on Soluble Poly(Thienylene Vinylene) Derivatives. *Org. Electron.* **2008**, *9*, 740–746.
- (19) Kim, J. Y.; Qin, Y.; Stevens, D. M.; Ugurlu, O.; Kalihari, V.; Hillmyer, M. A.; Frisbie, C. D. Low Band Gap Poly(Thienylene Vinylene)/Fullerene Bulk Heterojunction Photovoltaic Cells. *J. Phys. Chem. C* **2009**, *113*, 10790–10797.

- (20) Yang, G.; Hu, K.; Qin, Y. Cis/Cis-2,5-Dipropenylthiophene Monomers for High-Molecular-Weight Poly(2,5-Thienylene Vinylene) S through Acyclic Diene Metathesis Polymerization. *J. Polym. Sci., Part A: Polym. Chem.* **2014**, *52*, 591–595.
- (21) Gao, Y.; Martin, T. P.; Thomas, A. K.; Grey, J. K. Resonance Raman Spectroscopic- and Photocurrent Imaging of Polythiophene/Fullerene Solar Cells. *J. Phys. Chem. Lett.* **2010**, *1*, 178–182.
- (22) Favors, R. N.; Jiang, Y.; Loethen, Y. L.; Ben-Amotz, D. External Raman Standard for Absolute Intensity and Concentration Measurements. *Rev. Sci. Instrum.* **2005**, *76*, 033108/1–033108/5.
- (23) Clark, J.; Silva, C.; Friend, R. H.; Spano, F. C. Role of Intermolecular Coupling in the Photophysics of Disordered Organic Semiconductors: Aggregate Emission in Regioregular Polythiophene. *Phys. Rev. Lett.* **2007**, *98*, 206406/1–206406/4.
- (24) Spano, F. C.; Silva, C. H- and J-Aggregate Behavior in Polymeric Semiconductors. *Annu. Rev. Phys. Chem.* **2014**, *65*, 477–500.
- (25) Yamagata, H.; Spano, F. C. Interplay between Intrachain and Interchain Interactions in Semiconducting Polymer Assemblies: The H_j-Aggregate Model. *J. Chem. Phys.* **2012**, *136*, 184901/1–184901/14.
- (26) Ozaki, M.; Ehrenfreund, E.; Benner, R. E.; Barton, T. J.; Yoshino, K.; Vardeny, Z. V. Dispersion of Resonant Raman Scattering in Π -Conjugated Polymers: Role of the Even Parity Excitons. *Phys. Rev. Lett.* **1997**, *79*, 1762–1765.
- (27) Mevellec, J. Y.; Buisson, J. P.; Lefrant, S.; Eckhard, H.; Jen, K. Y. Theoretical Analysis of the Raman Spectra of PTV and PFV. *Synth. Met.* **1990**, *35*, 209–13.
- (28) Gao, J.; Thomas, A. K.; Johnson, R.; Guo, H.; Grey, J. K. Spatially Resolving Ordered and Disordered Conformers and Photocurrent Generation in Intercalated Conjugated Polymer/Fullerene Blend Solar Cells. *Chem. Mater.* **2014**, *26*, 4395–4404.
- (29) Reber, C.; Zink, J. I. Resonance Raman Deenhancement Caused by Excited-State Potential Surface Crossing. *J. Phys. Chem.* **1992**, *96*, 571–6.
- (30) Shin, K. S. K.; Zink, J. I. Interference Effects on Resonance Raman Excitation Profiles Caused by Two Electronic Excited States. *J. Am. Chem. Soc.* **1990**, *112*, 7148–57.
- (31) Tannor, D. J.; Heller, E. J. Polyatomic Raman Scattering for General Harmonic Potentials. *J. Chem. Phys.* **1982**, *77*, 202–18.
- (32) Heller, E. J.; Sundberg, R.; Tannor, D. Simple Aspects of Raman Scattering. *J. Phys. Chem.* **1982**, *86*, 1822–33.
- (33) Gao, J.; Grey, J. K. Resonance Raman Overtones Reveal Vibrational Displacements and Dynamics of Crystalline and Amorphous Poly(3-Hexylthiophene) Chains in Fullerene Blends. *J. Chem. Phys.* **2013**, *139*, 044903/1–044903/9.
- (34) Rich, C. C.; McHale, J. L. Resonance Raman Spectra of Individual Excitonically Coupled Chromophore Aggregates. *J. Phys. Chem. C* **2013**, *117*, 10856–10865.
- (35) Gao, Y.; Martin, T. P.; Niles, E. T.; Wise, A. J.; Thomas, A. K.; Grey, J. K. Understanding Morphology-Dependent Polymer Aggregation Properties and Photocurrent Generation in Polythiophene/Fullerene Solar Cells of Variable Compositions. *J. Phys. Chem. C* **2010**, *114*, 15121–15128.
- (36) Vandewal, K.; Tvingstedt, K.; Gadisa, A.; Inganaes, O.; Manca, J. V. On the Origin of the Open-Circuit Voltage of Polymer-Fullerene Solar Cells. *Nat. Mater.* **2009**, *8*, 904–909.
- (37) Louarn, G.; Mevellec, J. Y.; Lefrant, S.; Buisson, J. P.; Fichou, D.; Teulade-Fichou, M. P. Raman Study of A-Oligothiophenes and Model Compounds of Poly(Thienylenevinylene). *Synth. Met.* **1995**, *69*, 351–2.